EDGE ARTICLE

Modulatory spin-flip of triplet excitons *via* diversiform electron-donating units for MR-TADF emitters towards solution-processed narrowband OLEDs†

Shengyu Li,[a] Zhi Yang,[a] Yanchao Xie,[a] Lei Hua,[b] Shian Ying, [iD][a] Yuchao Liu, [iD] *[a] Zhongjie Ren[c] and Shouke Yan*[ac]

Multiple resonance thermally activated delayed fluorescence (MR-TADF) molecules are emerging as promising candidates for high-resolution organic light-emitting diode (OLED) displays, but MR-TADF emitters always suffer from an unsatisfactory rate constant of reverse intersystem crossing (k_{RISC}) due to inherently low spin orbital coupling strength between excited singlet and triplet states. Herein, we systematically investigate the long-range charge transfer (LRCT) and heavy-atom effects on modulating the excited state natures and energy levels *via* integrating diversiform electron-donating units with the MR skeleton. Compared with unsubstituted analogues, newly designed MR-TADF emitters exhibit significantly boosted k_{RISC} values and close-to-unity photoluminescence quantum yield especially for *t*BuCzBN-PXZ (2.5×10^5 s^{-1}) and *t*BuCzBN-Ph-PSeZ (2.1×10^5 s^{-1}). Leveraging these exceptional properties, the maximum external quantum efficiency values of *t*BuCzBN-PXZ- and *t*BuCzBN-Ph-PSeZ-based solution-processed OLEDs can reach 21.3% and 19.4%, which are in the first tier of reported solution-processed MR-TADF binary OLEDs without employing additional sensitizers. This study provides a framework for modulating photoelectrical properties of MR-TADF emitters through fastidiously regulating LRCT and heavy-atom effects.

Introduction

Thermally activated delayed fluorescence (TADF) emitters have been regarded as some of the most promising emitting materials for organic light-emitting diodes (OLEDs) due to simultaneously harvesting electro-generated singlet and triplet excitons and reaching a near-unity internal quantum efficiency.[1–6] Traditionally, a small singlet–triplet splitting energy (ΔE_{ST}) between the lowest excited singlet state (S_1) and triplet state (T_1) is a prerequisite to constructing TADF molecules, and thus dark T_1 excitons can be effectively harvested *via* the endothermic reverse intersystem crossing (RISC) process.[7–10] Although the spatially separated donor–acceptor (D–A) architectures in

conformist TADF molecules can attain small enough ΔE_{ST} values by minimizing the overlap between the highest occupied molecular orbital (HOMO) and the lowest unoccupied molecular orbital (LUMO), the inherent intramolecular charge transfer (ICT) characteristic together with inevitable structure relaxation in the excited states undesirably induce broadband emission with full width at half maximum (FWHM) exceeding 70 nm, and thus limiting the further utilization in high-resolution displays.[11–15] In this case, Hatakeyama and coworkers initially proposed an innovative molecular designing concept of multiple resonance (MR)-TADF emitters,[16] in which the frontier molecular orbitals (FMOs) are atomically separated through rationally positioning electron-donating (nitrogen or oxygen) and electron-accepting (boron) atoms into a polycyclic aromatic skeleton. Consequently, a narrowed emission band (FWHM < 30 nm) and evident TADF character can be achieved simultaneously.[17–22]

However, MR-TADF emitters always suffer from an unsatisfactory rate constant of RISC (k_{RISC}) of the order of only 10^4 s^{-1} because of inherently low spin orbital coupling (SOC) strength between S_1 and T_1 excited states.[20,23,24] As a result, the slow RISC process will induce exciton aggregation quenching behavior, such as triplet–triplet annihilation (TTA) and singlet–triplet annihilation (STA), especially under high current density in

[a]*Department Key Laboratory of Rubber-Plastics, Ministry of Education/Shandong Provincial Key Laboratory of Rubber-Plastics, School of Polymer Science and Engineering, Qingdao University of Science & Technology, Qingdao 266042, P. R. China. E-mail: liuyc@qust.edu.cn; skyan@qust.edu.cn*

[b]*School of Materials Science & Engineering, Changzhou University, Changzhou 213164, P. R. China*

[c]*State Key Laboratory of Chemical Resource Engineering, College of Materials Science and Engineering, Beijing University of Chemical Technology, Beijing 100029, P. R. China*

OLEDs, which can hinder exciton utilization and damage stability of devices. Although the hyperfluorescence mechanism can enable quick consumption of triplet excitons to suppress exciton annihilations *via* employing a TADF sensitizer with fast k_{RISC} as a mediator,[25–27] ternary hyperfluorescence OLEDs comprising host, emitter and sensitizer are confronted with complicated device fabrication procedure and relatively high device operation voltages. In this regard, to facilitate the RISC process is still in high demand for designing superior MR-TADF emitters.

According to the description of Fermi's golden rule, k_{RISC} can be strengthened by reducing ΔE_{ST} and enhancing SOC.[28,29] Nevertheless, the atomically localized FMOs of MR-TADF molecules hinder the further reduction of ΔE_{ST} through optimizing the molecular architecture resembling D–A type TADF compounds.[2,3,15,30] That is, the enhancement of SOC is deemed to be a feasible approach to accelerate k_{RISC}, and therefore, state-of-the-art MR-TADF emitters with improved k_{RISC} values have been proposed by delicately modulating excited state natures or resorting to the heavy-atom effect.[24,31–37] For instance, Yang and coworkers introduced an extra-long-range charge transfer (LRCT) state by installing a well-chosen electron-donating moiety to a polycyclic aromatic skeleton at the *para* position to a boron atom.[31] A multichannel RISC pathway with large SOC is established without disturbing the MR character of the S_1 state, and thus affording significantly increased k_{RISC} values and close-to-unity photoluminescence quantum yield (PLQY). Then they synergistically exploited LRCT and heavy-atom effect to accelerate k_{RISC} in designing MR-TADF emitters, demonstrating an attractive k_{RISC} of 2.2×10^6 s^{-1} and enabling low-efficiency roll-off in OLEDs.[38]

Although synergistic LRCT and the heavy-atom effect have been preliminarily investigated by incorporating a phenoselenazine (PSeZ) moiety into the MR framework, the photoelectric properties of MR-TADF emitters are only regulated by manipulating the substitution pattern (*para* and *meta* position of boron atoms). From the perspective of chemical structure, the electron-donating ability of additional donor moiety and spacer group can significantly affect the functionality of LRCT. Moreover, donor moieties with other large atomic numbers such as sulfur atom are also crucial to the accomplishment of large SOC strength.[39,40] In this context, it is quite indispensable to systematically investigate LRCT and heavy-atom effects on modulating the excited state natures and energy levels for designing high-efficiency MR-TADF emitters. Herein, three MR-TADF emitters were accessed by decorating the MR segment (*t*BuCzBN) with different donor moieties of phenoxazine (PXZ), phenothiazine (PTZ) and PSeZ, namely ***t*BuCzBN-PXZ**, ***t*BuCzBN-PTZ**, and ***t*BuCzBN-PSeZ**. Then the LRCT strength was delicately manipulated by inserting a phenyl bridge between MR segment and donor moieties, and thus we gained another three MR-TADF emitters denoted as ***t*BuCzBN-Ph-PXZ**, ***t*BuCzBN-Ph-PTZ**, and ***t*BuCzBN-Ph-PSeZ**. The molecular designing concept of these MR-TADF emitters is depicted in Scheme 1. Their photophysical characteristics were systematically studied, and careful quantum chemical calculations were performed, showcasing that the excited state na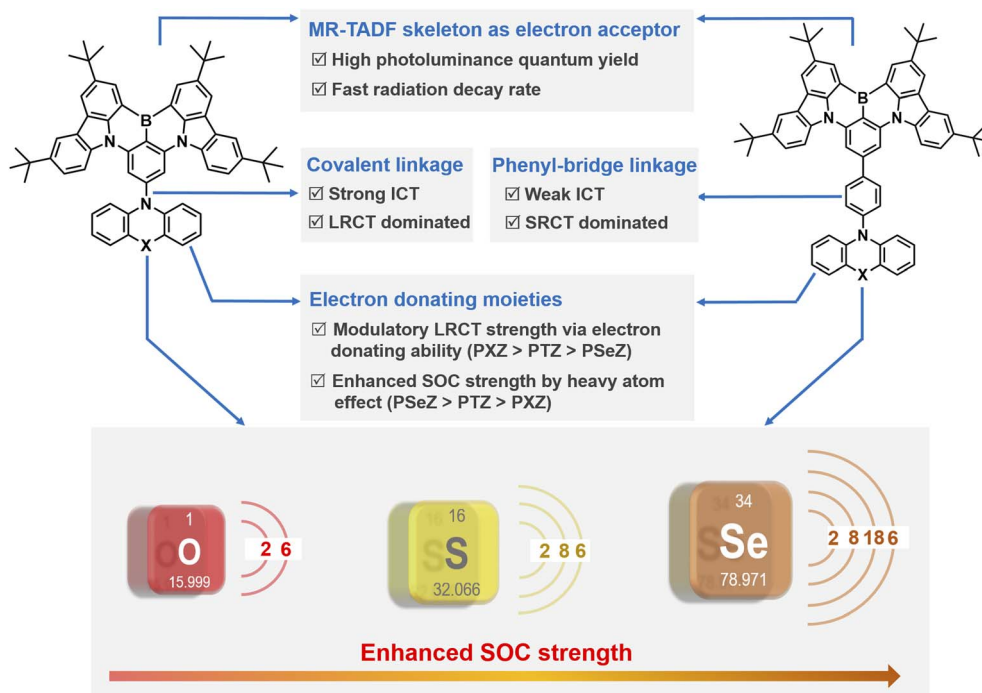tures and exciton radiative decay avenues are susceptible to the donor moieties. Compared with unsubstituted analogue *t*BuCzBN, these MR-TADF emitters exhibit significantly boosted k_{RISC} and attractive PLQY values, especially for ***t*BuCzBN-PXZ** (2.5×10^5 s^{-1}) and ***t*BuCzBN-Ph-PSeZ** (2.1×10^5 s^{-1}). Theoretical calculations together with photophysical studies also unambiguously manifest that the increased LRCT can induce an enhancement of k_{RISC}, in particular with respect to MR-TADF emitters decorated with relatively intense electron-donating units, and the heavy-atom effect can accelerate spin flip of triplet excitons *via* greatly enhanced SOC in the absence of a modulatory LRCT state. These deductions are also confirmed by EL performance in sensitizer-free solution-processed OLEDs, demonstrating excellent maximum external quantum efficiency (EQE$_{max}$) values of 21.3% and 19.4% for ***t*BuCzBN-PXZ** and ***t*BuCzBN-Ph-PSeZ**, respectively, which are in the first tier of reported solution-processable MR-TADF binary OLEDs.

Results and discussion

The detailed synthetic routes of these emitters are shown in Schemes S1–S12 of the ESI.† The chemical structures of the resultant emitters were characterized by ^{1}H NMR, ^{13}C NMR, and mass spectrometry (Fig. S1–S30†). We conducted thermogravimetric analysis (TGA), and all the emitters exhibited decomposition temperatures (T_d) of over 430 °C (Fig. S31†), verifying good thermal stability that benefits fabrication and operation of OLED devices. Firstly, we evaluated the FMOs of electron-donating units (Fig. S32†), and the HOMO values were determined to be −4.78, −5.05 and −5.07 eV for PXZ, PTZ and PSeZ, respectively, revealing the electron-donating ability of these fragments (PXZ > PTZ > PSeZ; Ph-PXZ > Ph-PTZ > Ph-PSeZ), which have been also verified by surface electrostatic distribution analyses as shown in Fig. S33.† Therefore, our design concept follows three considerations: (1) the introduction of LRCT can be accomplished by integrating electron-donating moieties with the MR skeleton; (2) the LRCT strength can be meticulously modulated by diversiform electron-donating units comprising PXZ, PTZ, PSeZ, Ph-PXZ, Ph-PTZ, and Ph-PSeZ, which are in descending order of electron-donating ability; (3) the effects of heavy atom on triplet exciton spin-flip in MR-TADF emitters featuring various LRCT strengths are also evaluated by employing donor moieties with the atomic number from oxygen to sulfur and selenium (Scheme 1).

Then quantum chemical simulations were performed to investigate the geometrical and electronic structures of these emitters at the molecular level calculated by density functional theory (DFT) at the M06-2X/6-311G** level of theory using Gaussian 16.[41,42] As shown in Fig. 1, these emitters reveal extremely distinct FMO distributions: ***t*BuCzBN-PXZ** shows FMO distributions similar to those of conventional D–A-type TADF emitters as expected, in which HOMOs are located on the PSeZ moiety, and the LUMOs are distributed over the MR skeleton. Similarly with ***t*BuCzBN-Ph-PXZ**, the HOMOs are located on the PSeZ moiety, while the LUMOs are delocalized on the MR skeleton and phenyl bridge. The extended FMOs not only result in lower energy gap (E_g) between HOMO and LUMO

Scheme 1 Molecular designing concept of MR-TADF emitters in this study.

levels of 4.73 eV for ***t*BuCzBN-Ph-PXZ** than that of 4.82 eV for ***t*BuCzBN-PXZ**, but also can maintain the LRCT effect between donor moiety and MR emitting core. For ***t*BuCzBN-PTZ**, the LUMOs are still localized in the MR skeleton, while the HOMOs are mainly located on the PTZ moiety and partly expanded to the MR skeleton, potentially signifying attenuated LRCT between donor moiety and MR emitting core. In contrast, the HOMOs

and LUMOs of ***t*BuCzBN-Ph-PTZ** are mainly distributed over the MR skeleton except a spot of HOMO distribution on the PTZ unit, featuring a nearly MR-type FMO configuration. In the cases of ***t*BuCzBN-PSeZ** and ***t*BuCzBN-Ph-PSeZ**, typical MR-type FMO configurations have been demonstrated, in which the HOMOs and LUMOs are almost localized by nitrogen and boron atoms, which can be ascribed to the relatively weak electron-
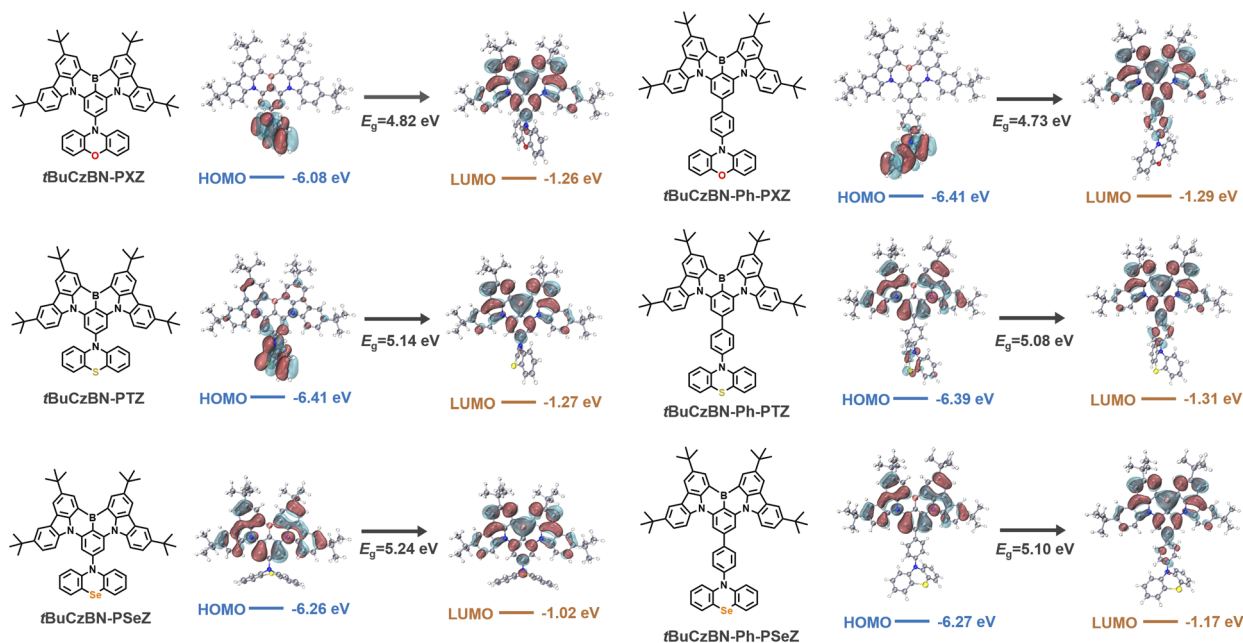

Fig. 1 The molecular structures of emitters and the FMO distributions. The corresponding energy levels and E_g values are shown in the diagrams.

donating ability as mentioned above. We also studied the calculated ground-state dipole moments of these emitters (Fig. S34†), which are all in the range of 2.03–3.11 debyes, with little noticeable changes for different MR-TADF emitters, signifying that ground-state dipole moments hardly affect the exciton decay behaviors. In terms of molecular conformation, for example, *t*BuCzBN-PXZ displays totally different exciton decay behaviors compared with *t*BuCzBN-PTZ despite the fact that both MR-TADF emitters exhibit quite similar molecular architecture including molecular conformations and dihedral angles.

The photophysical properties of the obtained emitters were evaluated in dilute toluene (1×10^{-5} M) using ultraviolet-visible (UV-vis) absorption and photoluminescence (PL) spectra at room temperature. As shown in Fig. 2a and b, all emitters exhibit conspicuous signals peaking at 450–470 nm, which experimentally confirm the presence of an intense ICT process. The signals below 400 nm can be assigned to the $n–\pi^*$ and $\pi–\pi^*$ transitions of the molecular backbone. From the onset band of UV-vis absorption, the E_g values between HOMO and LUMO levels can be determined to be 2.56, 2.56 and 2.59 eV for *t*BuCzBN-PXZ, *t*BuCzBN-PTZ and *t*BuCzBN-PSeZ, while the E_g values tend to be relatively smaller, 2.51, 2.51 and 2.52 eV, for *t*BuCzBN-Ph-PXZ, *t*BuCzBN-Ph-PTZ and *t*BuCzBN-Ph-PSeZ, respectively, after inserting the phenyl bridge between MR segment and donor moieties. Combined with the cyclic voltammetry results (Fig. S35†), the HOMO and LUMO values can be determined to be −5.59/−3.03 eV for *t*BuCzBN-PXZ, −5.62/−3.06 eV for *t*BuCzBN-PTZ, −5.57/−2.98 eV for *t*BuCzBN-PSeZ, −5.36/−2.85 eV for *t*BuCzBN-Ph-PXZ, −5.54/−3.03 eV for *t*BuCzBN-Ph-PTZ, −5.50/−2.98 eV for *t*BuCzBN-Ph-PSeZ, respectively.

From the PL spectra, all emitters exhibit similar emission profiles with small FWHM of <25 nm. As depicted in Fig. 2a, the maximum emission peaks exhibit discernible hypochromic shift with changing donor moieties from *t*BuCzBN-PXZ (480

nm) to *t*BuCzBN-PTZ (478 nm) and *t*BuCzBN-PSeZ (474 nm), preliminarily revealing the mediator effect of LRCT on excited states. Correspondingly, the emission peaks of *t*BuCzBN-Ph-PXZ, *t*BuCzBN-Ph-PTZ and *t*BuCzBN-Ph-PSeZ are mainly located at ≈490 nm (Fig. 2b). The similar emission peaks of these emitters basically signify limited LRCT strength between MR segment and donor moieties, which provides a platform to investigate the heavy-atom effect on modulating the excited states regardless of the LRCT effect.[37,43,44] As the ΔE_{ST} value is a prerequisite for maintaining valid spin flip of triplet excitons, we therefore determined the energy splitting of these emitters. The energies of S_1 and T_1 states can be estimated from the onset of fluorescence and phosphorescence spectra in toluene at 77 K, providing calculated ΔE_{ST} values of 0.05, 0.06 and 0.07 eV for *t*BuCzBN-PXZ, *t*BuCzBN-PTZ and *t*BuCzBN-PSeZ, respectively, which represent a gradual increase with increasing atomic number from oxygen to sulfur and selenium in donor moieties. Conversely, ΔE_{ST} values are decreasing for *t*BuCzBN-Ph-PXZ (0.05 eV), *t*BuCzBN-Ph-PTZ (0.02 eV) and *t*BuCzBN-Ph-PSeZ (0.02 eV). These small ΔE_{ST} values can ensure the establishment of effective channels for the triplet-to-singlet RISC process.

Furthermore, solvatochromic tests were performed to analyze the S_1 state properties of these emitters (Fig. 3). According to the solvatochromic effect of *t*BuCzBN-PXZ, *t*BuCzBN-PTZ and *t*BuCzBN-PSeZ (Fig. 3a–c), three emitters display narrow PL spectra at ≈469 nm with FWHM of 19 nm in non-polar hexane, indicating that these emissive states are close in energy level. On increasing the solvent polarity to highly polar dichloromethane, the high-energy emission spectra display a finite bathochromic shift of <28 nm for *t*BuCzBN-PXZ, <14 nm for *t*BuCzBN-PTZ and <12 nm for *t*BuCzBN-PSeZ, revealing the dominant emissive state feature short-range charge transfer (SRCT) characteristics contributed by the MR effect. Besides the high-energy sharp emission band, the PL spectrum of *t*BuCzBN-PXZ also possesses a low-energy broad emission band even in non-polar hexane. Comparatively, the solvatochromic effect for
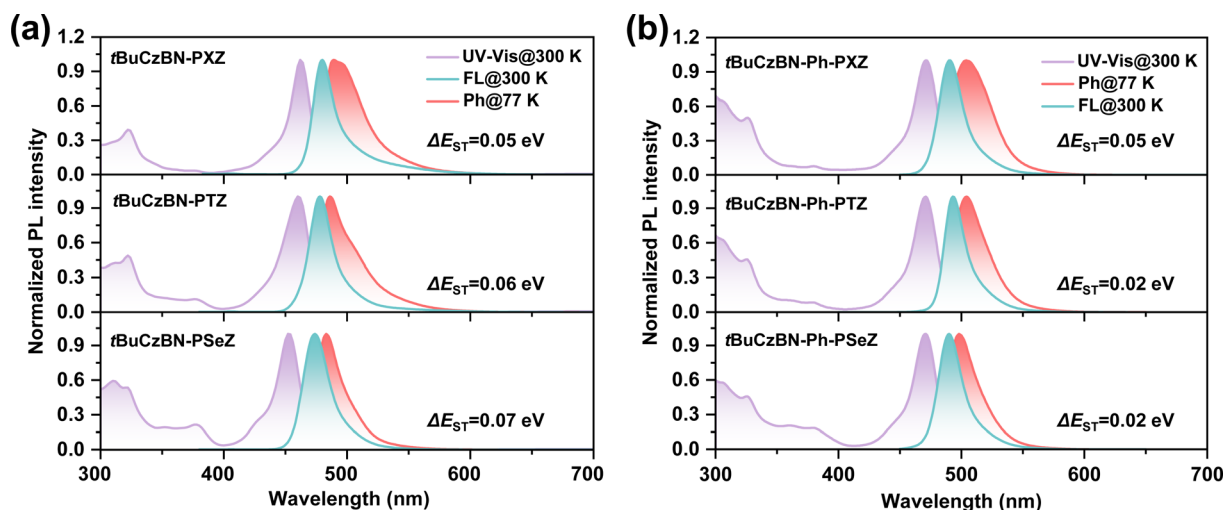

Fig. 2 The ultraviolet-visible absorption spectra and PL spectra of (a) *t*BuCzBN-PXZ, *t*BuCzBN-PTZ, and *t*BuCzBN-PSeZ diluted in toluene; (b) *t*BuCzBN-Ph-PXZ, *t*BuCzBN-Ph-PTZ, and *t*BuCzBN-Ph-PSeZ diluted in toluene.
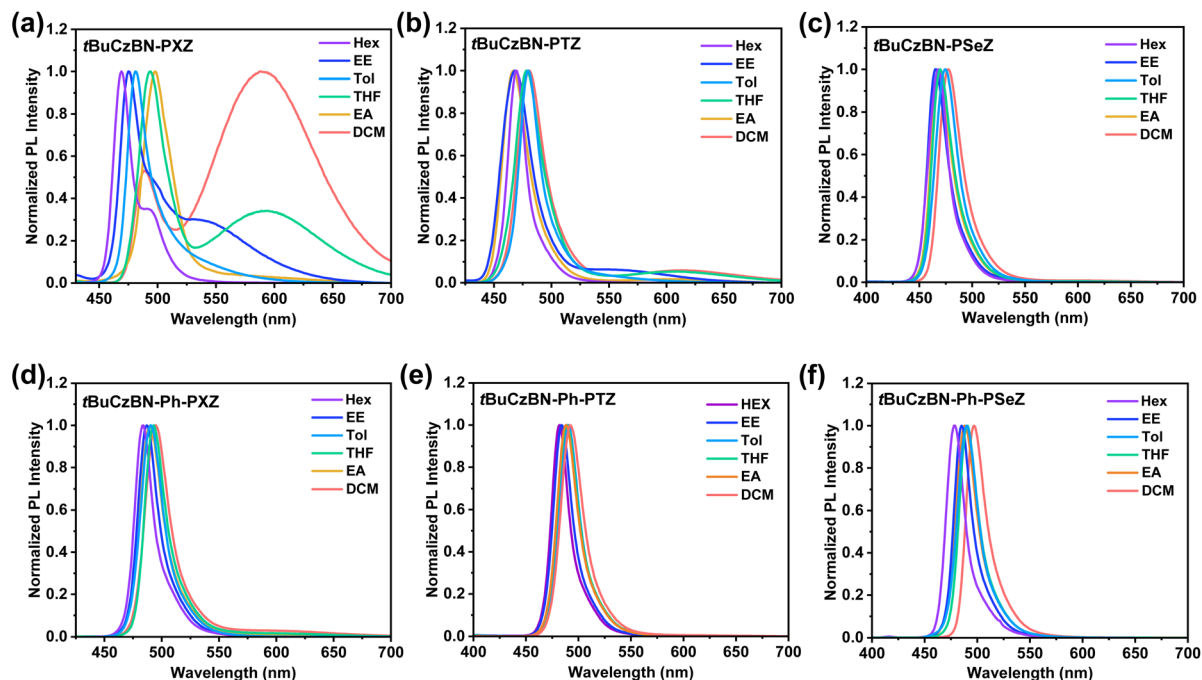
Fig. 3 Solvatochromic effect on PL spectra in 10^{-5} M solution. (a) *tBuCzBN-PXZ*, (b) *tBuCzBN-PTZ*, (c) *tBuCzBN-PSeZ*, (d) *tBuCzBN-Ph-PXZ*, (e) *tBuCzBN-Ph-PTZ* and (f) *tBuCzBN-Ph-PSeZ*. Hex: *n*-hexane; EE: diethyl ether; Tol: toluene; THF: tetrahydrofuran; EA: ethyl acetate; DCM: dichloromethane.

the low-energy emission peak is more noticeable with a bathochromic shift of ≈100 nm by altering solvent from hexane to dichloromethane, which clearly demonstrates that the strong electron-donating PXZ moiety induces the formation of a low-lying LRCT state. Similarly, the PL spectrum of *tBuCzBN-PTZ* also manifests dual emission comprising a sharp emission band at 467–481 nm and a perceptible broad emission band at 550–613 nm. Nevertheless, *tBuCzBN-PSeZ* only displays a single narrowband emission without any appendant LRCT emission, which can be ascribed to the relatively weak electron-donating ability of the PSeZ moiety. In sharp contrast, the PL spectrum of *tBuCzBN-Ph-PXZ* displays a sharp emission band at 483–495 nm together with faint LRCT emission while *tBuCzBN-Ph-PTZ* and *tBuCzBN-Ph-PSeZ* exhibit only a sharp emission band at 479–497 nm (Fig. 3d–f), emphasizing a feeble LRCT effect of these emitters. From the abovementioned fluorescence emission, it is evident that the LRCT effect can not only be modulated by electron-donating moieties (*tBuCzBN-PXZ* > *tBuCzBN-PTZ* > *tBuCzBN-PSeZ*), but also be effectively restrained by inserting a phenyl bridge between MR segment and donor moieties (*tBuCzBN-PXZ* > *tBuCzBN-Ph-PXZ*; *tBuCzBN-PTZ* > *tBuCzBN-Ph-PTZ*; *tBuCzBN-PSeZ* > *tBuCzBN-Ph-PSeZ*). The excited states are also investigated through the analysis of solvation effect by the Lippert-Mataga solvatochromic model (Fig. S36†). For *tBuCzBN-PXZ*, the hybrid LRCT and SRCT characteristics can be observed with dipole moments of 22.46 and 12.07 debyes, respectively. In addition, there exists only one single linear relationship with calculated dipole moments of 6.55, 5.91, 5.26, 4.75 and 7.23 debyes, respectively, for *tBuCzBN-PTZ*, *tBuCzBN-PSeZ*, *tBuCzBN-Ph-PXZ*, *tBuCzBN-Ph-PTZ* and

tBuCzBN-Ph-PSeZ, representing typical SRCT states. Overall, in terms of the S_1 state, all these MR-TADF emitters exhibit dominant SRCT natures, assuredly inheriting narrowband emission of the MR core.

To evaluate the exciton decay kinetics of these emitters, we recorded transient PL decay spectra of emitters blended into 9-(2-(9-phenyl-9*H*-carbazole-3-yl)phenyl)-9*H*-3,9′-bicarbazole (PhCzBCz) matrix in vacuum. All these transient PL spectra demonstrate bi-exponential decay, containing nanosecond-scale prompt fluorescence (PF) and microsecond-scale delayed fluorescence (DF) components (Fig. 4a), which afford compelling evidence of typical TADF characteristic for these emitters.[45,46] The corresponding prompt (τ_{PF}) and delayed (τ_{DF}) lifetimes were fitted to be 11.0 ns/6.8 μs for *tBuCzBN-PXZ*, 11.2 ns/7.7 μs for *tBuCzBN-PTZ*, 13.7 ns/7.9 μs for *tBuCzBN-PSeZ*, 11.2 ns/15.8 μs for *tBuCzBN-Ph-PXZ*, 11.6 ns/16.0 μs for *tBuCzBN-Ph-PTZ*, and 13.0 ns/16.9 μs for *tBuCzBN-Ph-PSeZ*, respectively. Additionally, the proportions of DF component (ϕ_{DF}) are dynamically tunable by altering the electron-donating moieties: 41% for *tBuCzBN-PXZ*, 34% for *tBuCzBN-PTZ*, 31% for *tBuCzBN-PSeZ*, 51% for *tBuCzBN-Ph-PXZ*, 53% for *tBuCzBN-Ph-PTZ*, and 72% for *tBuCzBN-Ph-PSeZ*. Thus, it can be preliminarily concluded that radiative decay and exciton upconversion avenues are susceptible to the LRCT and heavy-atom effect. Noteworthily, these emitters demonstrate not only significantly shortened τ_{DF} and boosted ϕ_{DF} values compared with unsubstituted analogue *tBuCzBN* (65.0 μs and 20%), but also close-to-unity PLQY values (Φ_{PL}). All of these photophysical properties are summarized in Table 1.
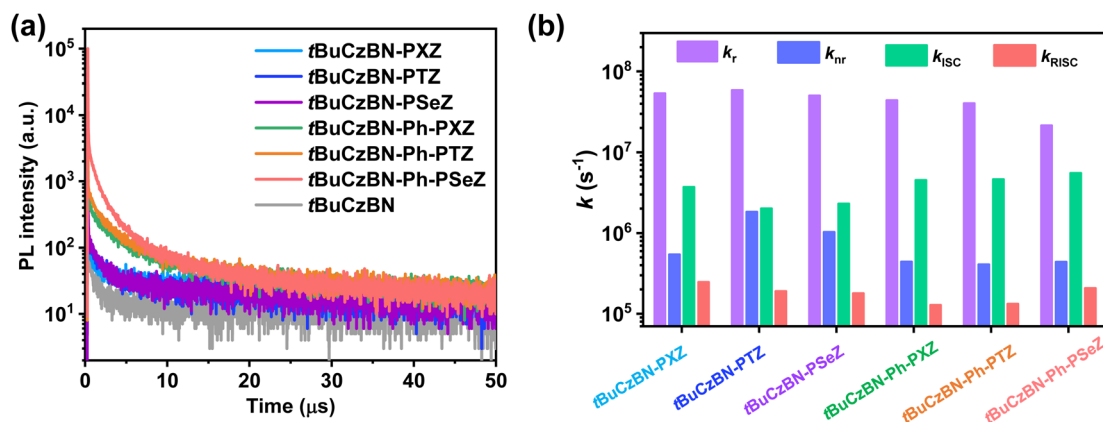
Fig. 4 (a) Transient PL decay curves of the emitters blended into matrix in vacuum; (b) comparison between the calculated rate constants.

Table 1 The photophysical properties of emitters

Emitter	λ_{abs}^{a} [nm]	λ_{PL}^{b} [nm]	FWHM^{c} [nm]	ΔE_{ST}^{d} [eV]	Φ_{PL}^{e} [%]	τ_p/τ_d^{f} [ns]/[μs]	φ_{DF}^{g} [%]	k_r^{Sh} [10^7 s^{-1}]	k_{RISC}^{i} [10^5 s^{-1}]	k_{ISC}^{j} [10^6 s^{-1}]
*t*BuCzBN-PXZ	323, 462	480	20	0.05	99	11.0/6.8	41	5.4	2.5	3.7
*t*BuCzBN-PTZ	322, 460	478	21	0.06	97	11.2/7.7	34	5.9	1.9	3.0
*t*BuCzBN-PSeZ	310, 453	474	24	0.07	98	13.7/7.9	31	5.0	1.8	2.3
*t*BuCzBN-Ph-PXZ	326, 471	490	23	0.05	99	11.2/15.8	51	4.4	1.3	4.5
*t*BuCzBN-Ph-PTZ	325, 471	492	20	0.02	99	11.6/16.0	53	4.0	1.4	4.6
*t*BuCzBN-Ph-PSeZ	326, 471	490	23	0.02	98	13.0/16.9	72	2.2	2.1	5.5

[a] Absorption peaks of emitters diluted in toluene. [b] Maximum emission peaks of emitters diluted in toluene. [c] Full width at half maximum. [d] Energy splitting between S_1 and T_1 determined from fitting the line of temperature-k_{RISC}. [e] Photoluminescence quantum yields of doped films. [f] The lifetimes of prompt fluorescence component and the lifetimes of delayed fluorescence component. [g] The proportion of delayed fluorescence component. [h] The rate constants of nonradiative decay for singlet excitons by equation $k_r^S = (1 - \varphi_{DF})/\tau_p$. [i] The rate constants of reverse intersystem crossing process calculated by equation $k_{RISC} = \Phi_{PL}/[\tau_d(1 - \varphi_{DF})]$. [j] The rate constants of intersystem crossing process calculated by equation $k_{ISC} = \varphi_{DF}/(\Phi_{PL}\tau_p)$.

To characterize the spin-flip processes quantitatively, we summarized k_{RISC} and the rate constants of radiative transition (k_r), nonradiative transition (k_{nr}), and intersystem crossing (k_{ISC}) as depicted in Fig. 4b. The k_{RISC} values are 2.5×10^5 s^{-1}, 1.9×10^5 s^{-1} and 1.8×10^5 s^{-1} for *t*BuCzBN-PXZ, *t*BuCzBN-PTZ and *t*BuCzBN-PSeZ, respectively, which can be ascribed to the decreased electron-donating ability of donor moieties (PXZ > PTZ > PSeZ) and subsequently decreasing LRCT strength, suggesting that the increased LRCT will induce an enhancement of k_{RISC} despite that heavy atoms can potentially strengthen the SOC between singlet and triplet excited states. Thus, it can be inferred that the LRCT plays a more crucial role than the heavy-atom effect in promoting k_{RISC}, in particular with respect to MR-TADF emitters decorated with relatively intense electron-donating units. Conversely, after inserting a phenyl bridge between MR segment and donor moieties, the k_{RISC} values are significantly increased when integrating heavy atoms into the emitters, especially for *t*BuCzBN-Ph-PSeZ with k_{RISC} of 2.1×10^5 s^{-1}, which evidently surpasses that of 1.4×10^5 s^{-1} for *t*BuCzBN-Ph-PTZ and 1.3×10^5 s^{-1} for *t*BuCzBN-Ph-PXZ. When the phenyl bridge is inserted between MR core and electron-donating unit, the LRCT effect will be weakened. Thus, it can be concluded that the heavy-atom effect (PXZ < PTZ < PSeZ)

plays a much more vital role than LRCT. Additionally, the k_r values of these MR-TADF emitters in blended films are of the order of 10^7 s^{-1} and significantly exceed the k_{nr} values (of the order of 10^5 to 10^6 s^{-1}), possibly due to their large oscillator strength (*f*) values. Furthermore, it should be noted that, with the reduced proportion of LRCT emission, non-radiative loss can be markedly suppressed, such as from 1.8×10^6 s^{-1} for *t*BuCzBN-PTZ to 4.1×10^5 s^{-1} for *t*BuCzBN-Ph-PTZ, demonstrating that SRCT state provided by the MR-type skeleton is conducive to strong electronic interactions, which are hardly achieved for a D–A-type TADF emitter due to the inherent separated D–A structure. Moreover, the k_{ISC} values are also determined to be (2.3–3.7) $\times$ 10^6 s^{-1} for *t*BuCzBN-PXZ, *t*BuCzBN-PTZ and *t*BuCzBN-PSeZ, and then further increased for *t*BuCzBN-Ph-PXZ (4.5×10^6 s^{-1}), *t*BuCzBN-Ph-PTZ (4.6×10^6 s^{-1}) and *t*BuCzBN-Ph-PSeZ (5.5×10^6 s^{-1}). The noticeable enhancement of k_{ISC} values further proves that the heavy-atom effects can effectively strengthen the SOC between singlet and triplet excited states when inserting a phenyl bridge between MR segment and donor moieties.[47] We also note that the k_r values are orders of magnitude greater than competitive k_{ISC} values, thus reducing multiple spin-flip cycles between singlet and triplet excited states and suppressing the undesired

accumulation of excitons. Eventually, STA and TTA can be prevented effectively in these MR-TADF emitters.[48,49]

We also recorded steady-state PL spectra of 2 wt% and 5 wt% MR-TADF emitters blended with PhCzBCz host materials. As shown in Fig. S37 and S38,† participations of triplet exciton gradually decline with decreasing electron-donating ability of donor moieties. Additionally, increasing doping concentrations of MR-TADF emitters in blended films can also suppress the participations of triplet exciton partly due to a more severe exciton quenching effect. To understand in depth the excited-state properties, we further studied the transient PL decay spectra of these emissive films with different doping concentrations (Fig. S39†). It is found that when the MR core is directly covalently linked with electron-donating moieties in both 2 wt% and 5 wt% MR-TADF emitter blended films, *t*BuCzBN-PXZ exhibits relatively faster exciton decay dynamic due to favorable LRCT effect. After inserting a phenyl bridge between MR core and donor moieties, *t*BuCzBN-Ph-PSeZ achieves much higher exciton decay rates and more participations of triplet exciton. Thus, it is concluded that the heavy-atom effect plays a much more vital role in suppressing LRCT strength. Moreover, the calculated k_{RISC} values, especially of *t*BuCzBN-PXZ in MR-TADF emitter blended films with high doping concentration, are lower than that in 1 wt% MR-TADF emitter blended films, potentially verifying the severe exciton–exciton annihilation. All the photophysical properties are summarized in Tables S1 and S2.†

To gain in-depth insights into the nature of excited states and upconversion process of the excitons, the excited-state energy levels and natural transition orbital (NTO) distributions of S_1 and T_n ($n = 1, 2$) were theoretically evaluated through time-dependent density functional theory (TD-DFT) calculations for these emitters by adopting the M06-2X functional with the 6-311G** basis set.[28,50] The SOC matrix elements (SOCME) of $\langle S_1|\hat{H}_{SO}|T_n\rangle$ between the T_n and S_1 states were calculated using the ORCA program. As evidenced by the NTO analysis (Fig. 5), the S_1 states of *t*BuCzBN-PXZ, *t*BuCzBN-PTZ and *t*BuCzBN-PSeZ exhibit MR-type FMO configurations, in which particle and hole are localized on separate atoms induced by nitrogen and boron atoms with extremely limited involvement of the donor units. Thus, the ensuing confined FMOs also curtail the vibronic coupling and excited-state structural relaxation, enabling an experimentally narrowed emission. Whereas, for *t*BuCzBN-Ph-PXZ, *t*BuCzBN-Ph-PTZ and *t*BuCzBN-Ph-PSeZ, the electron distributions are partly expanded to the phenyl bridge moieties. Although the delocalized FMOs result in relatively lower-lying S_1 energy level and corresponding bathochromic shift of emission peaks as described for PL spectra, the pronounced SRCT characters are expectedly retained. Furthermore, all molecules demonstrate attractive f values of 0.67–0.76, indicative of the SRCT nature of S_1 states, and enabling high k_r values of these MR-TADF emitters, which are well consistent with photophysical properties.

Notably, the estimated ΔE_{ST} values between S_1 and T_1 exceed 0.4 eV, which are always regarded as too large to implement favorable spin flip of triplet excitons. In addition, the S_1 and T_1 states of these emitters are accompanied by extremely similar

excited-state natures featuring SRCT characteristics, and therefore the corresponding SOCME values $\langle S_1|\hat{H}_{SO}|T_1\rangle$ are as low as 0.01–0.04 cm^{-1}, except for *t*BuCzBN-PSeZ with relatively high $\langle S_1|\hat{H}_{SO}|T_1\rangle$ of 0.11 cm^{-1} partly due to the quite limited involvement of the PSeZ unit. A higher-lying T_2 close to S_1 with promising energy differences of 0.01–0.11 eV is also noted. Considering the energetic proximity of S_1 and T_2, it can be anticipated that the T_2 states serve as intermediate states in the SOC interaction between singlet and triplet excited states, and thus the newly built conversion channels can be engaged synergistically to accelerate the spin-flip of triplet excitons and then to take charge of the unexpectedly excellent RISC dynamics.[51–53] More importantly, according to NTO distributions of T_2 states, these molecules display a comparatively distinct excited-state nature, in which *t*BuCzBN-PTZ, *t*BuCzBN-PSeZ and *t*BuCzBN-Ph-PTZ have SRCT character but a more locally excited triplet state (^{3}LE) component than relative T_1 states, signifying enhanced SOCME values $\langle S_1|\hat{H}_{SO}|T_2\rangle$ of 0.30–0.40 cm^{-1} compared with S_1–T_1. In sharp contrast, the T_2 state of *t*BuCzBN-PXZ displays detached NTO distributions in that the hole and particle are individually located on PSeZ donor and MR skeleton, respectively, manifesting a typical LRCT nature. Hence the SOCME value $\langle S_1|\hat{H}_{SO}|T_2\rangle$ of *t*BuCzBN-PXZ can reach 0.30 cm^{-1} even without the participation of heavy atoms, in line with excellent k_{RISC} value determined from transient decay spectra. From the above discussions, it is evident that integrating a donor moiety with fair electron-donating ability into the MR skeleton is a prerequisite for formation of a modulatory LRCT state, which plays an even more vital role than the heavy-atom effect in boosting a large SOC effect, and thus facilitating the RISC process.

In the case of the T_2 state of *t*BuCzBN-Ph-PXZ, the SOCME value $\langle S_1|\hat{H}_{SO}|T_2\rangle$ is only 0.04 cm^{-1}. The negligible SOCME value can be interpreted as the insulation of NTO-T_2 distribution from the MR skeleton since hole and particle are completely delocalized on the PXZ unit. In particular, the T_2 state of *t*BuCzBN-Ph-PSeZ exhibits an approximately mixed SRCT and LRCT nature as the hole distributions pervade the entire molecule while the particle distributions are mainly located on the MR skeleton and phenyl bridge. The hybrid excited-state nature together with a relatively prominent heavy-atom effect enable a significantly enhanced SOC between S_1 and T_2 states for *t*BuCzBN-Ph-PSeZ with $\langle S_1|\hat{H}_{SO}|T_2\rangle$ of as much as 0.63 cm^{-1}. As a consequence, the k_{RISC} value of 2.1×10^5 s^{-1} for *t*BuCzBN-Ph-PSeZ is very close to that of 2.5×10^5 s^{-1} for *t*BuCzBN-PXZ, disclosing that the heavy-atom effect can undoubtedly accelerate spin flip of triplet excitons *via* greatly enhanced SOC in the absence of modulatory LRCT state in MR-TADF emitters.

The atom force microscopy (AFM) results of all molecules (1 wt% MR-TADF doped in PhCzBCz) are shown in Fig. S40.† The relatively smooth surface topographies with a root mean square (RMS) surface roughness of 0.35–0.68 nm can be observed. There are no conspicuous voids and aggregates. These results demonstrate that the mixed systems have favorable film-formation abilities in luminous layer during solution-processed fabrication. To verify the potential of these MR-TADF emitters in electroluminescent (EL) devices, solution-
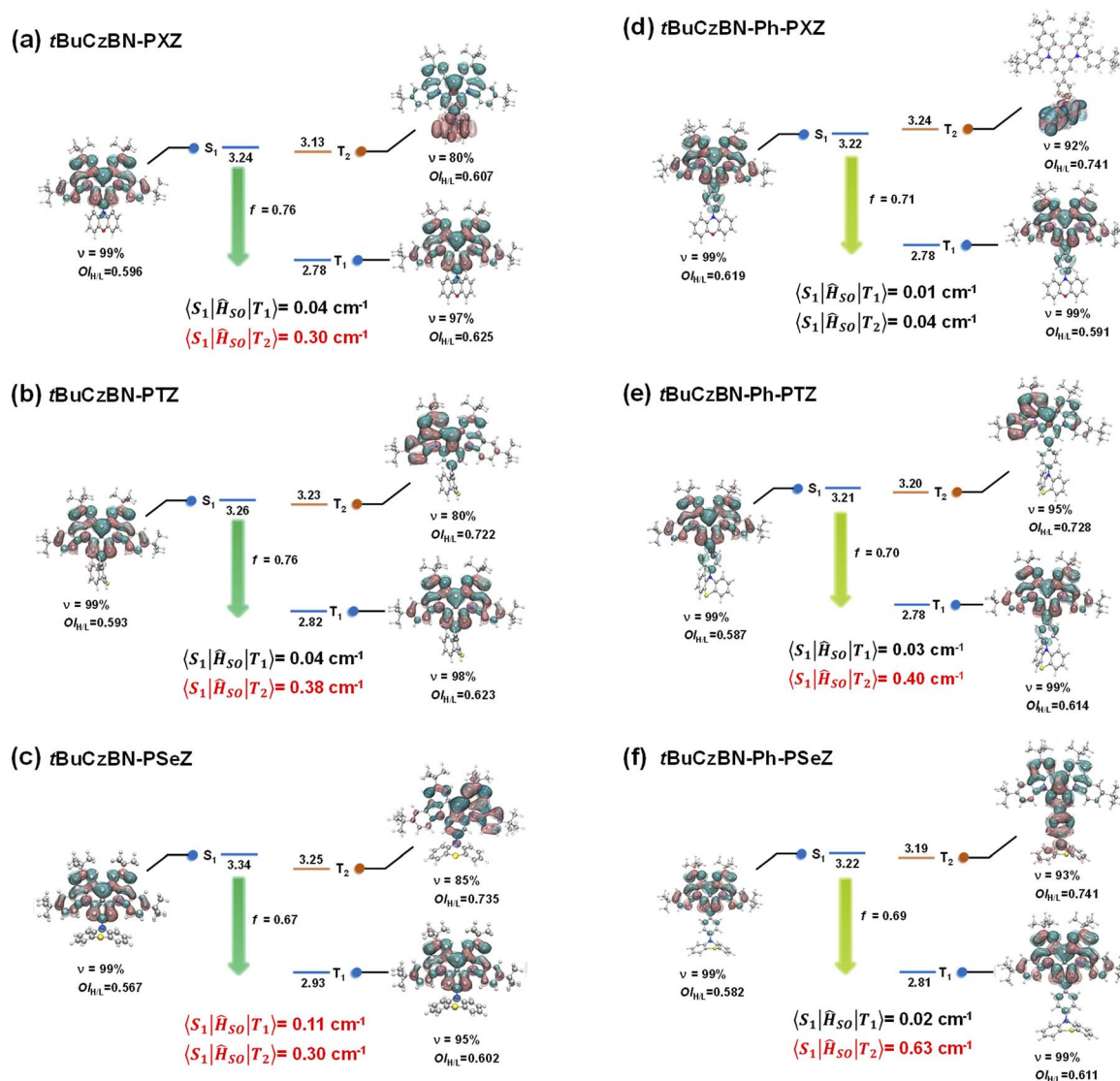
Fig. 5 Calculated energy-level diagrams, NTO distributions, and associated spin–orbit coupling (SOC) matrix elements for (a) tBuCzBN-PXZ, (b) tBuCzBN-PTZ, (c) tBuCzBN-PSeZ, (d) tBuCzBN-Ph-PXZ, (e) tBuCzBN-Ph-PTZ and (f) tBuCzBN-Ph-PSeZ.

processable OLEDs were fabricated with the architecture of ITO/ PSS:PEDOT (40 nm)/PVK (10 nm)/emitting layer (40 nm)/ TmPyPB (45 nm)/LiF (0.9 nm)/Al (110 nm) shown in Fig. 6a, where PSS:PEDOT, PVK, and TmPyPB are poly(3,4-ethylenedioxythiophene)-poly(styrene sulfonate), poly(9-vinylcarbazole), and 1,3,5-tri(m-pyridin-3-ylphenyl)benzene, respectively. PSS:PEDOT was adopted as hole injecting and transferring layer, and PVK and TmPyPB served as exciton-blocking and electron-transferring layers, respectively. For the emitting layer, the MR-TADF emitters were embedded into host materials of PhCzBCz, which could not only enhance the charge transferring capability, but also restrain the exciton quenching induced by molecular π–π accumulation, and the dopant concentration was optimized to be 1 wt%. From the current density–voltage–luminance (J–V–L) curves shown in Fig. 6b and c, the turn-on voltages (V_{on}) of devices are 3.8–4.4 V, in which the higher V_{on} value of tBuCzBN-Ph-PXZ can be ascribed to the shallower energy levels. Nearly all of the devices exhibit favorable maximum luminance (L_{max}) exceeding 1000 cd m^{-2}.

As depicted in Fig. 6d, the EL spectra of these devices are in great agreement with the PL profiles, especially for tBuCzBN-PXZ (480 nm), tBuCzBN-PTZ (478 nm) and tBuCzBN-PSeZ (474 nm) with a small FWHM of <30 nm. Slightly bathochromic shifts can be detected for tBuCzBN-Ph-PXZ (496 nm), tBuCzBN-Ph-PTZ (496 nm) and tBuCzBN-Ph-PSeZ (496 nm), and moreover, the FWHM values are unexpectedly increased to 33–36 nm, which should be attributed to the relatively larger transition dipole moment for these emitters and subsequently distinct solid-state solvation effect in high-polarity matrix. Additionally, all these devices exhibit excellent EL spectral stability as shown in Fig. S41.† The maximum current (CE$_{max}$) and power (PE$_{max}$) efficiencies are 41.9 cd A^{-1} and 29.9 lm W^{-1} for tBuCzBN-PXZ, which are correspondingly higher than that of 30.4 cd A^{-1} and 21.7 lm W^{-1} for tBuCzBN-PTZ, and 13.8 cd A^{-1} and 15.2 lm W^{-1}
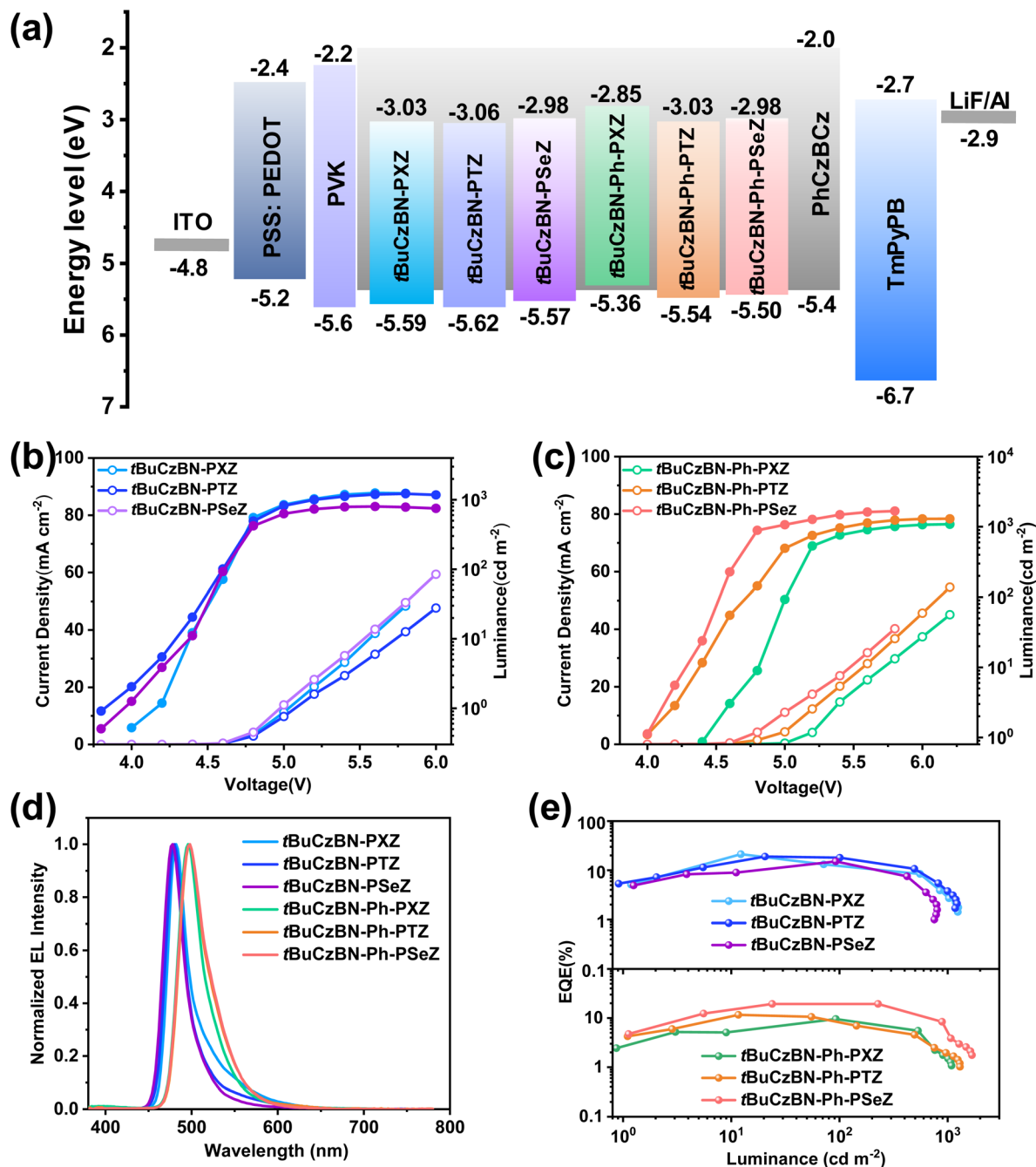
Fig. 6 (a) Device architecture and energy-level diagrams of the functional materials for solution-processed OLEDs. Current density and luminance *versus* voltage ($J-V-L$) characteristics for (b) *t*BuCzBN-PXZ, *t*BuCzBN-PTZ, and *t*BuCzBN-PSeZ; (c) *t*BuCzBN-Ph-PXZ, *t*BuCzBN-Ph-PTZ, and *t*BuCzBN-Ph-PSeZ. (d) EL spectra recorded at 6 V. (e) External quantum efficiency–luminance (EQE–L) plots.

for *t*BuCzBN-PSeZ, as illustrated in Fig. S42.† An important observation is that the solution-processable device performances based on these MR-TADF emitters match well with the corresponding photophysical properties, especially k_{RISC} values. Additionally, the CE_{max} and PE_{max} values of *t*BuCzBN-Ph-PSeZ are 50.5 cd A^{-1} and 26.0 lm W^{-1}, exceeding that of 23.0 cd A^{-1} and 14.4 lm W^{-1} for *t*BuCzBN-Ph-PXZ, and 30.1 cd A^{-1} and 21.5 lm W^{-1} for *t*BuCzBN-Ph-PSeZ, respectively. In line with the k_{RISC} values of these MR-TADF emitters in the film state, the EQE_{max}

value of *t*BuCzBN-PXZ can reach 21.3%, which is in the first tier of reported solution-processable MR TADF binary OLEDs without employing additional sensitizers (Fig. 6e). On decreasing the electron-donating ability of donor moieties, the EQE_{max} values are further reduced from 19.0% for *t*BuCzBN-PTZ to 15.2% for *t*BuCzBN-PSeZ, rationally validating that LRCT plays a more crucial role than the heavy-atom effect for MR-TADF emitters decorated with strong electron-donating units in promoting EL performance in solution-processable OLEDs.

Table 2 The EL properties of solution-processable OLEDs without TADF sensitizer

Emitter	V_{on}^a [V]	EL/FWHM^b [nm]	L_{max}^c [cd m^{-2}]	CE_{max}^d [cd A^{-1}]	PE_{max}^e [lm W^{-1}]	EQE_{max}^f [%]	CIE^g
tBuCzBN-PXZ	4.1	480/27	1255	41.9	29.9	21.3	(0.15, 0.32)
tBuCzBN-PTZ	3.9	478/28	1223	30.4	21.7	19.0	(0.14, 0.24)
tBuCzBN-PSeZ	3.8	474/29	801	20.3	13.8	15.2	(0.13, 0.20)
tBuCzBN-Ph-PXZ	4.4	496/33	1088	23.0	14.4	9.6	(0.13, 0.50)
tBuCzBN-Ph-PTZ	4.0	496/36	1301	30.1	21.5	11.6	(0.14, 0.52)
tBuCzBN-Ph-PSeZ	4.0	496/36	1677	50.5	26.0	19.4	(0.13, 0.51)

^{a} The turn-on voltages. ^{b} The electroluminescence spectral peaks and full width at half maximum determined at 6 V. ^{c} The maximum luminance. ^{d} The maximum current efficiencies. ^{e} The maximum power efficiencies. ^{f} The maximum external quantum efficiency. ^{g} The coordinates of CIE.

In contrast, the EQE_{max} value drops dramatically to only 9.6% after inserting a phenyl group between **tBuCzBN** MR segment and **PXZ** donor moieties (**tBuCzBN-Ph-PXZ**). Furthermore, the EQE_{max} values increase significantly to 11.6% for **tBuCzBN-Ph-PTZ** and even 19.4% for **tBuCzBN-Ph-PSeZ**, corroborating that the heavy-atom effect can enable exceptional EL performance when considering relatively limited LRCT and distinct SRCT effects in MR-TADF emitters. The EL properties of solution-processable OLEDs are summarized in Table 2.

We also fabricated solution-processed OLEDs with different doping concentration of 2 wt% and 5 wt% MR-TADF compounds diluted into PhCzBCz host materials. The device performances are summarized in Fig. S43, S44, and Tables S3, S4.† Comparatively, the device performance of 2 wt% MR-TADF-based OLEDs is better than that of 5 wt% MR-TADF-based OLEDs. More importantly, for both 2 wt% MR-TADF- and 5 wt% MR-TADF-based OLEDs, the EQE values are almost declining with decreasing electron-donating ability of donor moieties when directly covalently linking MR core with electron-donating moieties. In contrast, the EQE values will be enhanced on integrating a heavy atom, especially selenium atom, into the MR skeleton when inserting a phenyl bridge. Overall, the MR-TADF solution-processed OLEDs with different dopant concentrations not only prove the superior properties of these compounds, but also demonstrate our designing principle mentioned above. Actually, we also fabricated ternary MR-TADF solution-processable OLEDs with 1 wt% emitter, 10 wt% 5Cz-TRZ and 89 wt% PhCzBCz as emitting layer where 5Cz-TRZ as sensitizer is 9,9′,9″,9‴,9⁗-[6-(4,6-diphenyl-1,3,5-triazin-2-yl)-1,2,3,4,5-benzenepentayl]pentakis-9H-carbazole. The device performances are summarized in Fig. S45 and Table S5.† It is found that the ternary MR-TADF sensitized OLEDs have dramatically improved luminance, but the EQE values are lower than those of non-sensitized binary devices, which can be ascribed to the inefficient energy transfer from sensitizer to MR-TADF emitters or an uncompetitive exciton upconversion process.

Conclusions

In summary, we proposed a series of MR-TADF emitters by integrating diversiform electron-donating units with the MR skeleton to systematically investigate the LRCT and heavy-atom effects on modulating the excited-state natures and energy levels. The photophysical characteristics and careful quantum chemical calculations manifest that radiative decay and exciton upconversion avenues are susceptible to the modulation of electron-donating moieties. For MR-TADF emitters, in which the MR segments are covalently linked with electron-donating moieties, the excited-state characteristics can be delicately manipulated by the electron-donating ability. Especially for **tBuCzBN-PXZ**, enhanced LRCT can facilitate spin-flip of triplet excitons, and thus dramatically accelerating the RISC process while maintaining narrowed emission of the S_1 state. It has also been demonstrated that LRCT represents a more notable advantage than heavy-atom effects in prompting exciton dynamics for MR-TADF emitters decorated with relatively intense electron-donating units. By contrast, the LRCT strength has been further weakened after inserting a phenyl bridge between MR segment and donor moieties. According to the photophysical properties and quantum chemical simulation results, the noticeable enhancement of k_{RISC} values with increased atom numbers indicates that the heavy-atom effect can undoubtedly accelerate spin flip of triplet excitons via greatly enhanced SOC in the absence of modulatory LRCT state in MR-TADF emitters. Thus, both **tBuCzBN-PXZ** and **tBuCzBN-Ph-PSeZ** exhibit significantly boosted k_{RISC} values exceeding 2.0×10^5 s^{-1} and close-to-unity photoluminescence quantum yield. Leveraging these exceptional properties, the EQE_{max} values of **tBuCzBN-PXZ**- and **tBuCzBN-Ph-PSeZ**-based solution-processable OLEDs can reach 21.3% and 19.4% which are in the first tier of reported solution-processable MR TADF binary OLEDs without employing additional sensitizers. We believe that this study provides a framework for modulating photo-electrical properties of MR-TADF emitters through fastidiously regulating LRCT and heavy-atom effects.

Data availability

The data (experimental instrumentation, synthetic procedures, structural characterization data including NMR and MS spectra, theoretical calculations, thermodynamics data, and device performance data) that support this article are available in the article itself and its ESI.†

Author contributions

Li, S., Yang, Z., Xie, Y., Liu, Y. – conceptualization, investigation, OLED devices, writing – original draft; Li, S., Yang, Z., Xie, Y. – theoretical calculation, investigation; Li, S., Xie, Y. – formal

analysis, OLED devices; Li, S. – investigation (thermal properties); Li, S., Hua, L., Xie, Y. – investigation (transient PL properties); Liu, Y., Ren Z., Yan, S., Ying, S. – project administration, supervision; Liu, Y., Ren Z., Yan, S. – writing – review and editing.

Conflicts of interest

There are no conflicts to declare.

Acknowledgements

Notes and references

1 H. Uoyama, K. Goushi, K. Shizu, H. Nomura and C. Adachi, *Nature*, 2012, **492**, 234–238.

2 F. B. Dias, K. N. Bourdakos, V. Jankus, K. C. Moss, K. T. Kamtekar, V. Bhalla, J. Santos, M. R. Bryce and A. P. Monkman, *Adv. Mater.*, 2013, **25**, 3707–3714.

3 H. Liu, Y. Liu, G. Chen, Y. Meng, H. Peng, J. Miao and C. Yang, *Chem. Sci.*, 2024, **15**, 12598–12605.

4 W. Zeng, H. Y. Lai, W. K. Lee, M. Jiao, Y. J. Shiu, C. Zhong, S. Gong, T. Zhou, G. Xie and M. Sarma, *Adv. Mater.*, 2018, **30**, 1704961.

5 C. Li, A. K. Harrison, Y. Liu, Z. Zhao, C. Zeng, F. B. Dias, Z. Ren, S. Yan and M. R. Bryce, *Angew. Chem., Int. Ed.*, 2022, **134**, e202115140.

6 G. Meng, H. Dai, Q. Wang, J. Zhou, T. Fan, X. Zeng, X. Wang, Y. Zhang, D. Yang and D. Ma, *Nat. Commun.*, 2023, **14**, 2394.

7 Y. Liu, C. Li, Z. Ren, S. Yan and M. R. Bryce, *Nat. Rev. Mater.*, 2018, **3**, 1–20.

8 M. Y. Wong and E. Zysman-Colman, *Adv. Mater.*, 2017, **29**, 1605444.

9 Y. Tao, K. Yuan, T. Chen, P. Xu, H. Li, R. Chen, C. Zheng, L. Zhang and W. Huang, *Adv. Mater.*, 2014, **26**, 7931–7958.

10 X. Tang, L.-S. Cui, H.-C. Li, A. J. Gillett, F. Auras, Y.-K. Qu, C. Zhong, S. T. Jones, Z.-Q. Jiang and R. H. Friend, *Nat. Mater.*, 2020, **19**, 1332–1338.

11 L.-S. Cui, A. J. Gillett, S.-F. Zhang, H. Ye, Y. Liu, X.-K. Chen, Z.-S. Lin, E. W. Evans, W. K. Myers and T. K. Ronson, *Nat. Photon.*, 2020, **14**, 636–642.

12 D. Zhang, X. Song, A. J. Gillett, B. H. Drummond, S. T. Jones, G. Li, H. He, M. Cai, D. Credgington and L. Duan, *Adv. Mater.*, 2020, **32**, 1908355.

13 W. Yuan, H. Yang, C. Duan, X. Cao, J. Zhang, H. Xu, N. Sun, Y. Tao and W. Huang, *Chem*, 2020, **6**, 1998–2008.

14 Y. Liu, L. Hua, Z. Zhao, S. Ying, Z. Ren and S. Yan, *Adv. Sci.*, 2021, **8**, 2101326.

15 K. Shi, Y. Xie, L. Hua, S. Li, Z. Yang, Y. Yin, Z. Wang, S. Ying, Y. Liu and Z. Ren, *ACS Mater. Lett.*, 2024, **6**, 1491–1503.

16 T. Hatakeyama, K. Shiren, K. Nakajima, S. Nomura, S. Nakatsuka, K. Kinoshita, J. Ni, Y. Ono and T. Ikuta, *Adv. Mater.*, 2016, **28**, 2777–2781.

17 X.-C. Fan, K. Wang, Y.-Z. Shi, Y.-C. Cheng, Y.-T. Lee, J. Yu, X.-K. Chen, C. Adachi and X.-H. Zhang, *Nat. Photon.*, 2023, **17**, 280–285.

18 Y. Zhang, J. Wei, L. Wang, T. Huang, G. Meng, X. Wang, X. Zeng, M. Du, T. Fan and C. Yin, *Adv. Mater.*, 2023, **35**, 2209396.

19 Y. Zou, J. Hu, M. Yu, J. Miao, Z. Xie, Y. Qiu, X. Cao and C. Yang, *Adv. Mater.*, 2022, **34**, 2201442.

20 Y. Xu, C. Li, Z. Li, Q. Wang, X. Cai, J. Wei and Y. Wang, *Angew. Chem., Int. Ed.*, 2020, **59**, 17442–17446.

21 Y. Kondo, K. Yoshiura, S. Kitera, H. Nishi, S. Oda, H. Gotoh, Y. Sasada, M. Yanai and T. Hatakeyama, *Nat. Photon.*, 2019, **13**, 678–682.

22 P. Jiang, J. Miao, X. Cao, H. Xia, K. Pan, T. Hua, X. Lv, Z. Huang, Y. Zou and C. Yang, *Adv. Mater.*, 2022, **34**, 2106954.

23 Y. Zhang, G. Li, L. Wang, T. Huang, J. Wei, G. Meng, X. Wang, X. Zeng, D. Zhang and L. Duan, *Angew. Chem., Int. Ed.*, 2022, **61**, e202202380.

24 T. Hua, L. Zhan, N. Li, Z. Huang, X. Cao, Z. Xiao, S. Gong, C. Zhou, C. Zhong and C. Yang, *Chem. Eng. J.*, 2021, **426**, 131169.

25 D. Zhang and L. Duan, *Nat. Photon.*, 2021, **15**, 173–174.

26 Y. Wada, H. Nakagawa, S. Matsumoto, Y. Wakisaka and H. Kaji, *Nat. Photon.*, 2020, **14**, 643–649.

27 C.-Y. Chan, M. Tanaka, Y.-T. Lee, Y.-W. Wong, H. Nakanotani, T. Hatakeyama and C. Adachi, *Nat. Photon.*, 2021, **15**, 203–207.

28 P. K. Samanta, D. Kim, V. Coropceanu and J.-L. Brédas, *J. Am. Chem. Soc.*, 2017, **139**, 4042–4051.

29 M. K. Etherington, J. Gibson, H. F. Higginbotham, T. J. Penfold and A. P. Monkman, *Nat. Commun.*, 2016, **7**, 13680.

30 Y. Zhang, Z. Huang, Y. Yang, J. Liu, Y. Tian, Z. Bin and J. You, *Chem. Sci.*, 2023, **14**, 5125–5131.

31 Z. Huang, H. Xie, J. Miao, Y. Wei, Y. Zou, T. Hua, X. Cao and C. Yang, *J. Am. Chem. Soc.*, 2023, **145**, 12550–12560.

32 H.-J. Cheon, S.-J. Woo, S.-H. Baek, J. H. Lee and Y.-H. Kim, *Adv. Mater.*, 2022, **34**, 2207416.

33 Y. Xu, C. Li, Z. Li, Q. Wang, X. Cai, J. Wei and Y. Wang, *Angew. Chem., Int. Ed.*, 2020, **59**, 17442–17446.

34 Y. Liu, X. Xiao, Z. Huang, D. Yang, D. Ma, J. Liu, B. Lei, Z. Bin and J. You, *Angew. Chem., Int. Ed.*, 2022, **61**, e202210210.

35 Y. X. Hu, J. Miao, T. Hua, Z. Huang, Y. Qi, Y. Zou, Y. Qiu, H. Xia, H. Liu and X. Cao, *Nat. Photon.*, 2022, **16**, 803–810.

36 I. S. Park, H. Min and T. Yasuda, *Angew. Chem., Int. Ed.*, 2022, **61**, e202205684.

37 X. Cao, K. Pan, J. Miao, X. Lv, Z. Huang, F. Ni, X. Yin, Y. Wei and C. Yang, *J. Am. Chem. Soc.*, 2022, **144**, 22976–22984.

38 Y. Zou, M. Yu, Y. Xu, Z. Xiao, X. Song, Y. Hu, Z. Xu, C. Zhong, J. He and X. Cao, *Chem*, 2024, **10**, 1485–1501.

39 X. Tong, Z. Zhao, L. Hua, Y. Zhang, B. Xu, Y. Liu, S. Yan and Z. Ren, *Adv. Funct. Mater.*, 2023, **33**, 2305324.

40 I. S. Park, M. Yang, H. Shibata, N. Amanokura and T. Yasuda, *Adv. Mater.*, 2022, **34**, 2107951.

41 T. Lu and F. Chen, *J. Comput. Chem.*, 2012, **33**, 580–592.

42 T. Lu and F. Chen, *Acta Chim. Sinica*, 2011, **69**, 2393.

43 C. L. Kim, J.-M. Kim, H. Jang, D. R. Lee and Y. Lee, *ACS Appl. Energy Mater.*, 2022, **5**, 4985–4990.

44 D. R. Lee, K. H. Lee, W. Shao, C. L. Kim, J. Kim and J. Y. Lee, *Chem. Mater.*, 2020, **32**, 2583–2592.

45 S. Wu, W. Li, K. Yoshida, D. Hall, S. Madayanad Suresh, T. Sayner, J. Gong, D. Beljonne, Y. Olivier and I. D. Samuel, *ACS Appl. Mater. Interfaces*, 2022, **14**, 22341–22352.

46 Y. Xie, L. Hua, Z. Wang, Y. Liu, S. Ying, Y. Liu, Z. Ren and S. Yan, *Sci. China Chem.*, 2023, **66**, 826–836.

47 H. S. Kim, J. Y. Lee, S. Shin, W. Jeong, S. H. Lee, S. Kim, J. Lee, M. C. Suh and S. Yoo, *Adv. Funct. Mater.*, 2021, **31**, 2170374.

48 P. Han, C. Lin, H. Xu, E. Xia, D. Yang, A. Qin, D. Ma and B. Z. Tang, *ACS Mater. Lett.*, 2022, **4**, 1087–1093.

49 K. Matsuoka, K. Albrecht, K. Yamamoto and K. Fujita, *Sci. Rep.*, 2017, **7**, 41780.

50 M. K. Etherington, N. A. Kukhta, H. F. Higginbotham, A. Danos, A. N. Bismillah, D. R. Graves, P. R. McGonigal, N. Haase, A. Morherr and A. S. Batsanov, *J. Phys. Chem. C*, 2019, **123**, 11109–11117.

51 H. Noda, X.-K. Chen, H. Nakanotani, T. Hosokai, M. Miyajima, N. Notsuka, Y. Kashima, J.-L. Brédas and C. Adachi, *Nat. Mater.*, 2019, **18**, 1084–1090.

52 Y. Liu, L. Hua, S. Yan and Z. Ren, *Nano Energy*, 2020, **73**, 104800.

53 D. Liu, J. Y. Wei, W. W. Tian, W. Jiang, Y. M. Sun, Z. Zhao and B. Z. Tang, *Chem. Sci.*, 2020, **11**, 7194–7203.